NANO LETTERS

pubs.acs.org/NanoLett Letter

Sub-1K Cold-Electron Quantum Well Switching at Room Temperature

Anthony Martinez, Pushkar K. Gothe, Yi-De Liou, Ojas T. Bhayde, J. Tyler Gish, Vinod K. Sangwan, Michael P. Rabel, Thévenin Rumende, Gumaro G. Gonzalez, Jiechao Jiang, Ye Cao, Pierre Darancet, Efstathios Meletis, Mark C. Hersam, and Seong Jin Koh*

Cite This: *Nano Lett.* 2024, 24, 13981−13990 Read Online

ABSTRACT: Quantum states can provide means to systematically manipulate the transport of electrons. Here we present electron transport across quasi-bound states of two heterogeneous quantum wells (QWs), where the transport of thermally excited electrons is blocked or enabled depending on the relative positions of the two quasi-bound states, with an abrupt current onset occurring when the two QW states align. The QW switch comprises a source (Cr), QW1 (Cr_2O_3), QW2 (SnO_x, $x < 2$), a tunneling barrier (SiO_2), and a drain (Si), where the effective electron mass of QW1 (m^*_{QW1}) is selected to be larger than QW2 (m^*_{QW2}). The current−voltage (I−V) measurements of the fabricated devices show abrupt current onsets, with the current transition occurring within 0.25 mV, corresponding to an effective electron temperature of 0.8 K at room temperature. Since transistor power consumption is fundamentally tied to effective electron temperature, this sub-1K cold-electron QW switching holds promise for highly energy-efficient computing.

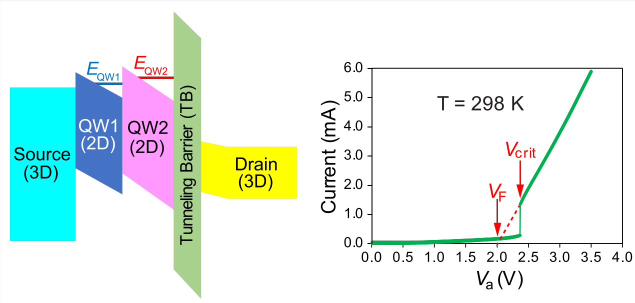

KEYWORDS: *electron tunneling, Fermi−Dirac thermal smearing, cold-electron transport, transverse momentum conservation, electron energy filtering, energy-efficient computing*

In electron systems at room temperature, the thermally excited hot electrons in the tail of the Fermi−Dirac distribution often lead to undesirable effects. For example, they can nullify Coulomb blockade in single-electron transport[1−5] and are responsible for the OFF-state leakage current in metal-oxide-semiconductor field-effect transistors (MOSFETs).[6−27] To mitigate these issues, a quantum state can be exploited as a spectral filter that enables electron transport only at specific energies, thereby blocking the transport of thermally excited hot electrons.[28−34] This strategy allows the cold transport of electrons in which the Fermi−Dirac thermal smearing is suppressed, thus lowering the effective electron temperature substantially below the reservoir temperature.

Quantum-state-mediated cold-electron transport has been experimentally demonstrated utilizing a single quantum state as an electron energy filter.[28−30,35,36] For example, a quantum dot (QD) created from the gate-confined 2-dimensional electron gas (2DEG) of a GaAs/AlGaAs layer was able to inject 0.03 K cold electrons to an adjacent QD at a reservoir temperature of 0.1 K.[28,29,35] It was also demonstrated that a single QW state created in a ∼2 nm Cr_2O_3 layer can act as an electron energy filter, resulting in the injection of 45 K cold electrons to a CdSe QD or a gold nanoparticle at room temperature.[30,36] Although these studies demonstrate the effectiveness of quantum states in manipulating the effective temperature of electrons involved in charge transport, significant improvements are required to realize electron transport with an effective electron temperature much closer to zero Kelvin (*e.g.*, below 1 K) at room temperature.

In this work, we demonstrate that the combination of quantum states from two heterogeneous QWs can efficiently filter electron transport, ultimately suppressing thermal smearing down to an effective electron temperature of 0.8 K at room temperature. The two heterogeneous QWs are selected to have different effective electron masses, with the effective electron mass of QW1 (m^*_{QW1}) being much larger than QW2 (m^*_{QW2}). We observe that these heterogeneous QWs effectively block electron transport before alignment of the field-induced quasi-bound states of QW1 and QW2, resulting in dramatic reductions of thermal smearing. When

Received: July 14, 2024
Revised: October 21, 2024
Accepted: October 22, 2024
Published: October 28, 2024

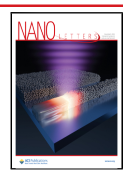

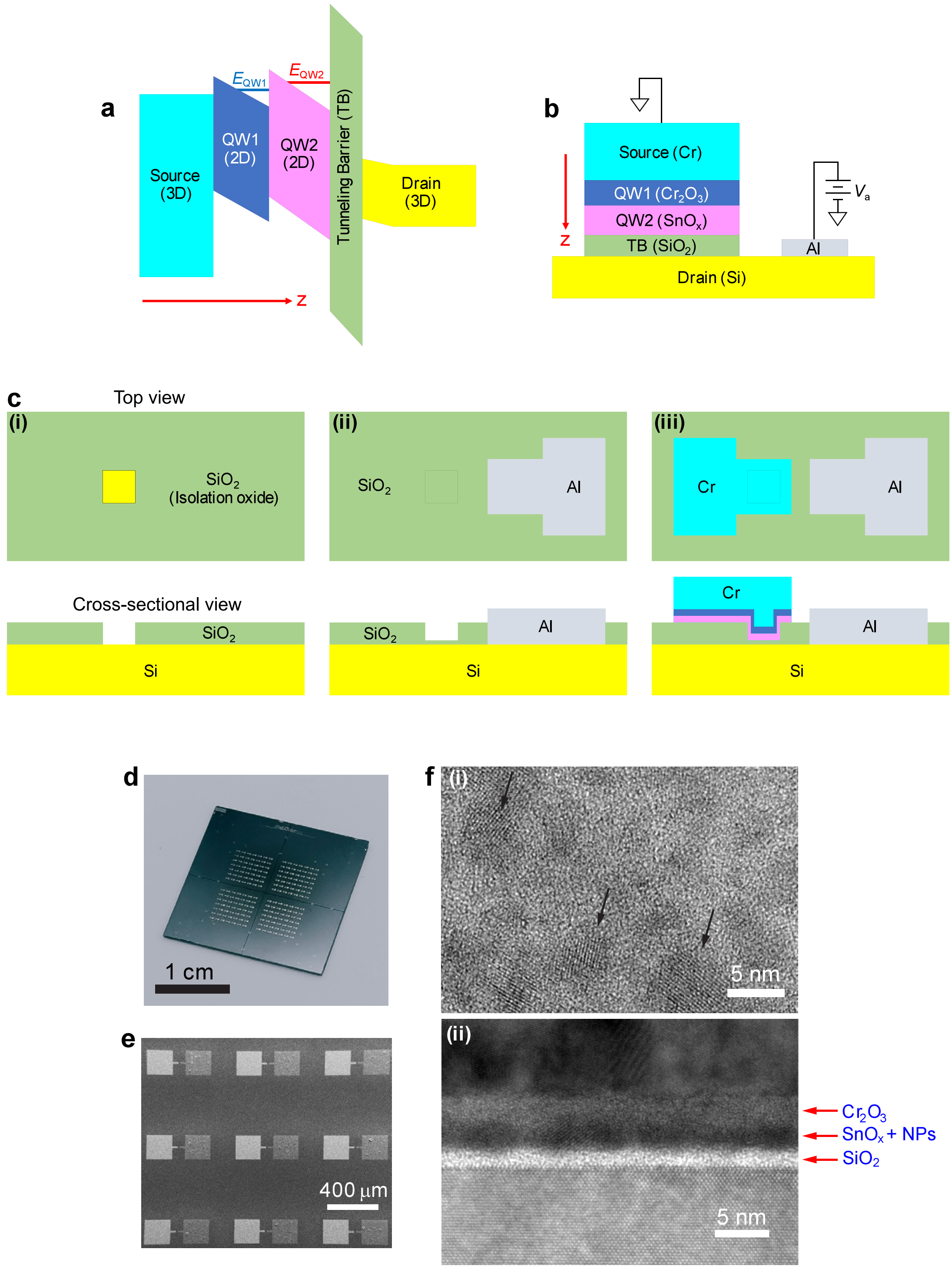

Figure 1. QW switching concept, device structure and fabrication. Schematics in (a)-(c) are not to scale. (a) An energy diagram (simplified) for QW switching. (b) A schematic of the device structure. (c) Fabrication procedure. (i) 1st photomask step. (ii) 2nd photomask step. (iii) 3rd photomask step. (d) A photograph of the fabricated devices. (e) SEM image of the fabricated devices. (f) Representative HRTEM images of the film stack. (i) Plan view of the QW2 (SnO_x) layer. Crystalline nanoparticles embedded in the SnO_x layer are indicated by arrows. (ii) Cross-sectional view.

the heterogeneous double QWs are placed between source and drain electrodes, they act as a switch (*i.e.*, blocking/enabling electron transport), particularly enabling an abrupt current onset without thermal smearing. This cold-electron QW switching is demonstrated with devices fabricated using high-yield CMOS-compatible processes.

The energy diagram in Figure 1a displays the concept of QW switching. The quasi-bound states of QW1 and QW2 (represented by E_{QW1} and E_{QW2}) are formed in two adjacent triangular QWs when voltage V_a is applied to the drain (with the source grounded).[31,32] Electrons in the source transfer through these heterogeneous QW states to reach the drain. When $E_{QW1} < E_{QW2}$, electron transport from QW1 to QW2 is

https://doi.org/10.1021/acs.nanolett.4c03348
Nano Lett. 2024, 24, 13981−13990

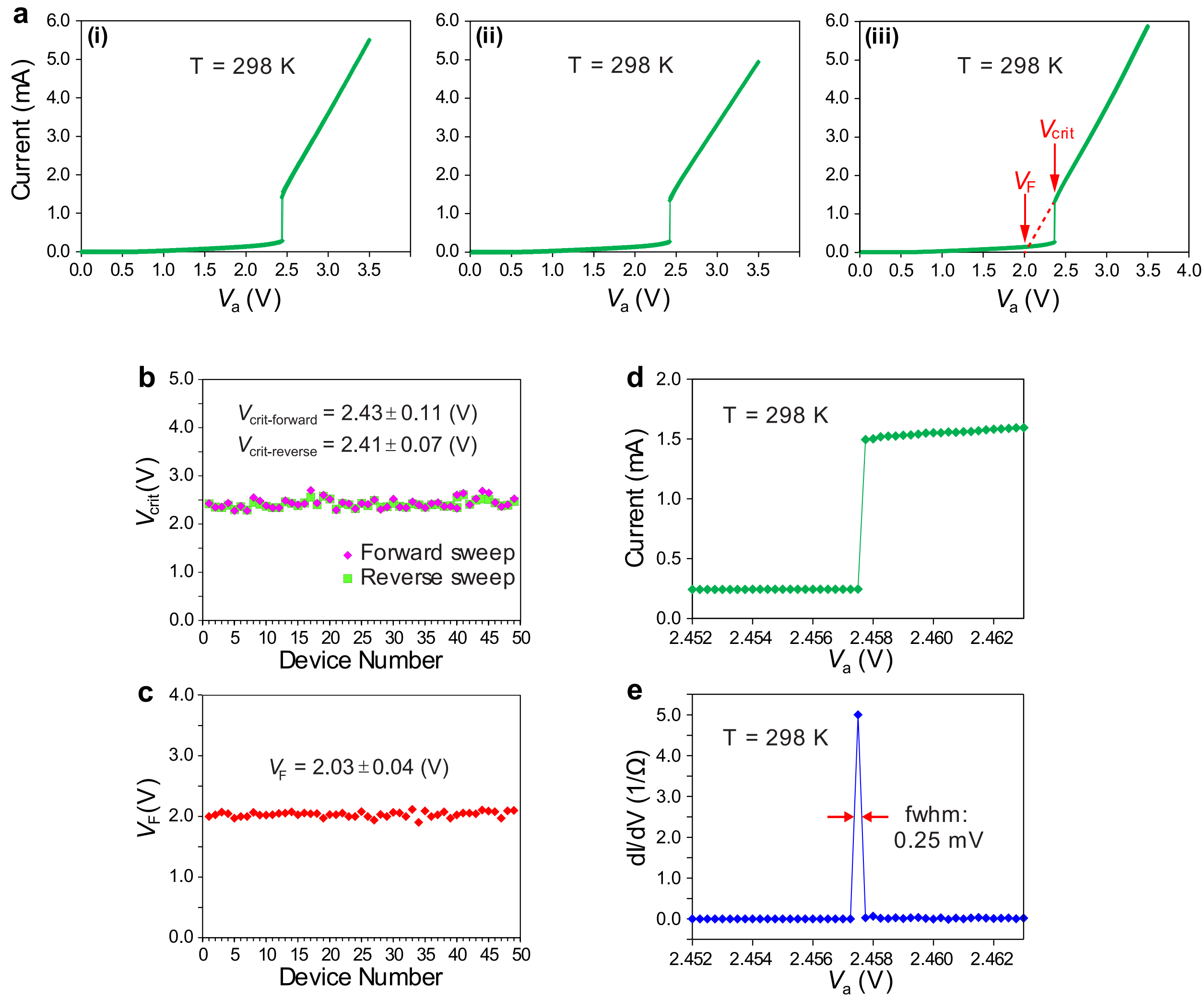

Figure 2. Electrical characteristics of the QW switching devices. All measurements were performed at room temperature. V_a: A voltage bias applied to the drain with the source grounded. (a) Representative *I-V* characteristics of the fabricated devices. V_{crit} and V_F are defined in (iii). (b-c) V_{crit} and V_F from 49 devices in a 7 × 7 device array, respectively. $V_{crit\text{-}forward}$ and $V_{crit\text{-}reverse}$: V_{crit} for forward sweep and reverse sweep, respectively. (d) *I-V* characteristics measured around V_{crit} at voltage resolution of 0.25 mV. (e) *dI/dV* characteristics numerically obtained from the *I-V* in (d).

blocked. When $E_{QW1} = E_{QW2}$, electron transport is allowed, and continually enabled as $E_{QW1} > E_{QW2}$. As we will now demonstrate experimentally, the blocking of electron transport when $E_{QW1} < E_{QW2}$ in our structure eliminates contributions of hot electrons in the source and leads to an abrupt current onset when E_{QW1} and E_{QW2} align, resulting in cold-electron QW switching at room temperature.

Figure 1b displays a schematic of the device structure that produces the energy configuration in Figure 1a. The device components are arranged in a vertical configuration (along the *z* direction). The devices were fabricated on a Si substrate (*p*-type Si (100); Boron doped at a concentration of ∼1.0 × 10^{15} [1/cm^3]; Sheet resistance: 1−25 Ω-cm) using CMOS-compatible processes that involved three photomask steps (see Supporting Information B). Figure 1c outlines the fabrication flow, which starts with a Si wafer on which 250 nm thick SiO_2 is thermally grown. Using the first photomask, windows are created inside the thermally grown SiO_2, exposing the Si substrate underneath, Figure 1c(i). The patterned wafer is then exposed to air (inside the class 1000 cleanroom) for more than 1 day to grow a native SiO_2 layer (∼2 nm) on the exposed Si areas. This native oxide layer is used as the tunneling barrier in Figures 1a-1b. The drain contact areas are defined using the second photomask, followed by 200 nm thick Al deposition, Figure 1c(ii). Then, the source contact areas are defined using the third photomask, and film stacks (50 nm Cr/1.5 nm Cr_2O_3/0.6 nm Cr/4 nm SnO_2) are deposited on those areas, Figure 1c(iii). Finally, the wafer is annealed at 490 °C for 5 min to reduce SnO_2 to SnO_x (see Supporting Information A and C).

Figures 1d and 1e show a photograph and a scanning electron microscopy (SEM) image of the fabricated devices, respectively. Figures 1**f(i)**-(ii) display representative HRTEM images (plan view and cross-sectional view) of the film stacks (see schematics of the microstructures in Figure S5). The plan view (Figure 1f(i)) shows an amorphous SnO_x layer with dispersed nanoparticles (NPs) having different sizes and compositions (Sn, Sn_2O_3, and Sn_3O_4) (see also Supporting Information C). We note that these nanoparticles are unlikely to be responsible for the QW switching characteristics to be presented below (Figure 2) because many nanoparticles with different sizes and compositions would have different electronic structures that would not lead to a single abrupt current jump if multiple nanoparticles were involved in charge

https://doi.org/10.1021/acs.nanolett.4c03348
Nano Lett. 2024, 24, 13981−13990

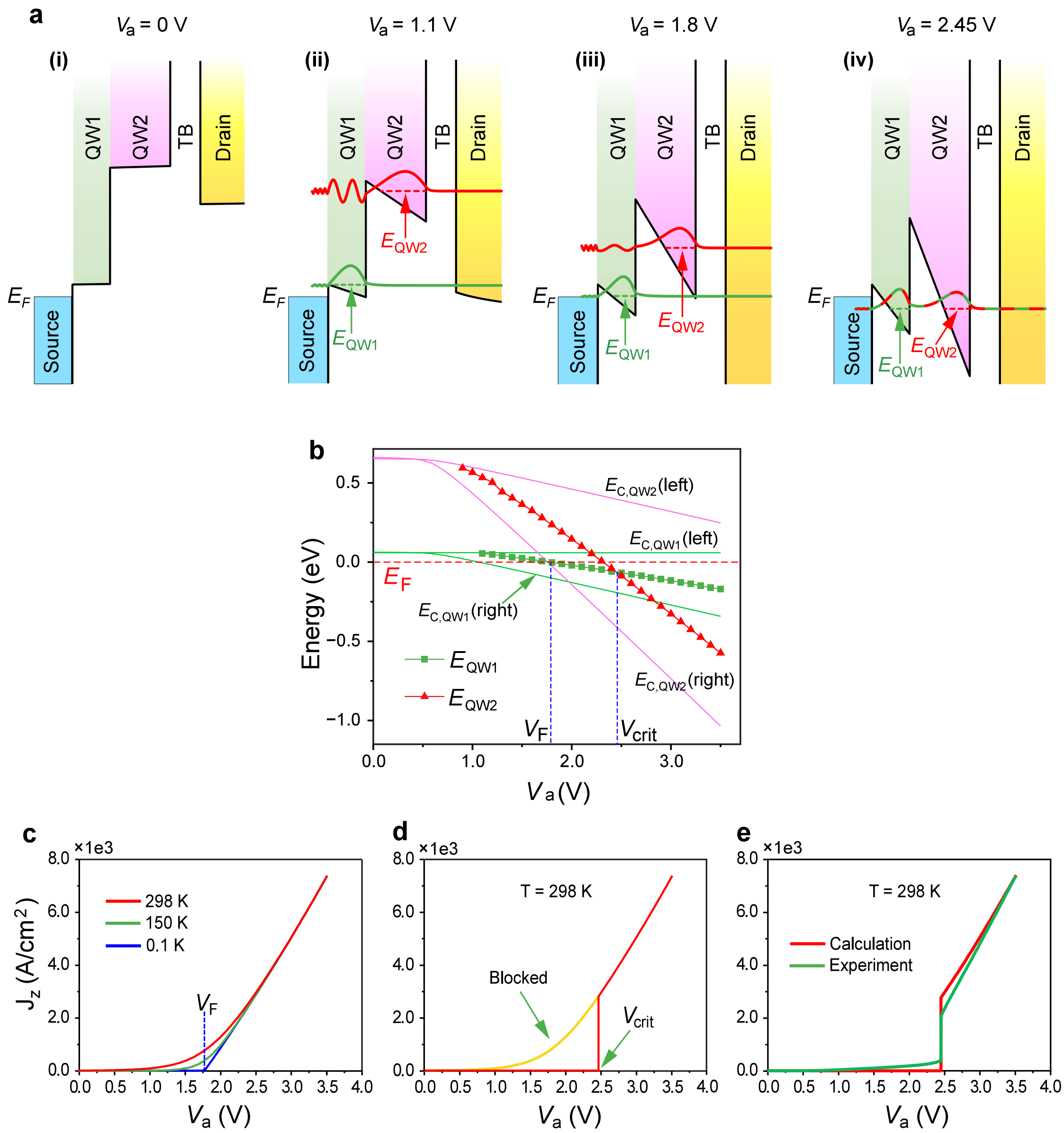

Figure 3. Modeling of cold-electron QW switching. (a) Calculated electron potential energy diagrams (only the conduction band edges E_C are shown), the eigenenergies of the quasi-bound states of QW1 and QW2 (E_{QW1} and E_{QW2}), and their wave functions at different applied voltages ((i)-(iv)). (b) Plot of E_{QW1} and E_{QW2} (green squares and red triangles, respectively) as a function of V_a. $E_{C,QW1}$ (left): Conduction band edge of QW1 at the source (Cr)/QW1 (Cr_2O_3) interface. $E_{C,QW1}$ (right): Conduction band edge of QW1 at the QW1 (Cr_2O_3)/QW2 (SnO_x) interface. $E_{C,QW2}$ (left): Conduction band edge of QW2 at the QW1 (Cr_2O_3)/QW2 (SnO_x) interface. $E_{C,QW2}$ (right): Conduction band edge of QW2 at the QW2 (SnO_x)/TB (SiO_2) interface. V_F: the V_a at which the E_F intersects with the E_{QW1}. V_{crit}: the V_a at which E_{QW1} intersects with E_{QW2}. (c) Calculated *J-V* characteristics for the source-QW1 (3D-2D) tunneling at different temperatures. (d) Calculated *J-V* characteristics (red line) with the QW switch inserted between the source and drain at room temperature. QW switch blocks electron tunneling when $V_a < V_{crit}$. (e) Comparison of the *J-V* curves between the experiment (green) and the calculation (red). The experimental *J-V* is from Figure 2a(i)).

transport. Furthermore, the magnitude of the measured current jump is in the milliampere range, which could not be accommodated by a single nanoparticle without physical damage.[37,38] These nanoparticles, however, can contribute to background currents.

The electrical characterization of the fabricated devices was carried out using current−voltage (*I-V*) measurements at room temperature. Figure 2a displays three representative *I-V* characteristics (see also Supporting Information D). Each shows an abrupt current jump at V_{crit} = ∼2.4 V, with the amount of current jump exceeding 1 mA. These *I-V* measurements were performed with cyclic voltage sweeps (forward voltage sweep from 0 to 3.5 V, followed by reverse sweep from 3.5 to 0 V) with minimal hysteresis. After the current jump at V_{crit} = ∼2.4 V, the current increases linearly with increasing V_a. This linear relationship originates from 3D-2D tunneling, from the source (3D) to the QW1 (2D) (Supporting Information G and H). Extrapolations of the linear *I-V* to the horizontal V_a axis show consistent values of ∼2.0 V, which we define as V_F (Figure 2a(iii)). In the later section below, we show that at $V_a = V_F$ the Fermi level of the source (E_F) aligns with the E_{QW1} of QW1.

Supporting Information D shows all *I-V* characteristics from a single batch (a total of 49 devices in a 7 × 7 device array).

The yield for this batch is 100% (meaning that all devices produced the abrupt current jump at V_{crit} = ∼2.4 V). Figure 2b shows the measured V_{crit} values from all 49 devices, demonstrating the consistency of the *I-V* characteristics. The V_{crit} values for the forward sweep ($V_{crit\text{-}forward}$) and the reverse sweep ($V_{crit\text{-}reverse}$) are displayed as pink diamonds and green squares, respectively. $V_{crit\text{-}forward}$ and $V_{crit\text{-}reverse}$ are measured to be 2.43 ± 0.11 (V) and 2.41 ± 0.07 (V), respectively, showing minimal hysteresis and device-to-device variation (see also Supporting Information J). Figure 2c displays V_F from all 49 devices, also showing minimal device-to-device variation.

The degree of abruptness in the current jump at V_{crit} is a measure of how effectively the Fermi−Dirac thermal smearing is eliminated. The abrupt current jumps shown in Figure 2a were further examined by carrying out *I-V* measurements at a higher voltage resolution, 0.25 mV, around V_{crit}. A representative *I-V* curve is shown in Figure 2d, which shows a current jump contained within the 0.25 mV resolution at V_{crit} (see also Figure S9). The corresponding differential conductance dI/dV (numerically obtained from the *I-V* in Figure 2d) is shown in Figure 2e. We find that the width of the differential conductance peak at V_{crit} is extremely narrow, with the full width at half-maximum (fwhm) at the voltage resolution limit of 0.25 mV (*i.e.*, 0.25 meV in energy units). For normal electron tunneling that occurs under Fermi−Dirac thermal smearing, the temperature dependence of the dI/dV fwhm has a linear relationship:[30,39]

$$\text{fwhm} = k_B T[\ln(3 + 2\sqrt{2}) - \ln(3 - 2\sqrt{2})] = 3.53 k_B T \quad (1)$$

where k_B is the Boltzmann constant and T is the absolute temperature. From eq 1, the measured fwhm of 0.25 mV in Figure 2e and Figure S9 corresponds to an effective electron temperature of 0.8 K. Because there are voltage divisions across the device components (QW1, QW2, SiO_2, and Si), the extracted value of 0.8 K is an upper bound of the effective electron temperature. We also want to note that the fwhm of 0.25 mV was limited by the voltage resolution of 0.25 mV of our instrument (Agilent E5287A). Measurement with a higher voltage resolution could lead to fwhm's smaller than 0.25 mV, therefore an effective electron temperature lower than 0.8 K.

We numerically calculated the energies of the quasi-bound states of QW1 and QW2 (E_{QW1} and E_{QW2}) as a function of V_a. In brief (details in Supporting Information F), we first solved the 1-D (along the z direction in Figure 1a) Poisson equation and charge transport equations for a given applied voltage V_a. A *p*-type Si with a dopant concentration of 1.0×10^{15} [1/cm^3] was used for the drain (other materials parameters in Supporting Information F). The solution of the coupled Poisson equation and charge transport equations (eqs (F1) - (F6) in the Supporting Information F) provides the electrical potential $V(z)$, electron density $n(z)$, hole density $p(z)$, conduction band edges $E_C(z)$, and valence band edges $E_V(z)$. With the electron potential energies ($E_C(z)$ and $E_V(z)$) obtained for a specific V_a, we numerically solved the Schrödinger equation, which provided the E_{QW1} and E_{QW2} for the QW1 and QW2, respectively. Assuming a sequential transport from the source to QW1 (T1), from QW1 to QW2 (T2), and from QW2 to the drain (T3), a proper alignment of E_{QW1} and E_{QW2} is a necessary (but not sufficient) condition to observe a current onset. Transport rates across the states of the device components (source, QW1, QW2, and drain) were evaluated, providing numerically calculated *I-V* characteristics (calculation details in Supporting Information F, G, and H).

Figures 3a(i-iv) show calculated electron potential energies (conduction band edges $E_C(z)$'s are shown), as well as the resulting QW energies (E_{QW1} and E_{QW2}) and their wave functions at different V_a. Figure 3a(i) shows the electron potential energies at V_a = 0, at which no QW states are formed. As V_a increases, band bending in the QW1 and QW2 layers increases, resulting in formation of triangular QWs and their quasi-bound states. Figures 3a(ii)-(iv) show the corresponding quasi-bound states of QW1 and QW2 at V_a = 1.1, 1.8, and 2.45 V (= V_{crit}), respectively. Figure 3b shows the positions of E_{QW1} and E_{QW2} at different V_a. We see that E_{QW2} (red triangles and line) decreases faster than E_{QW1} (green squares and line) as V_a increases. Both energy level lines intersect at the critical voltage V_{crit} = 2.45 V, where both energy levels E_{QW1} and E_{QW2} align. The calculated value of V_{crit} (2.45 V) agrees well with the measured value of 2.42 V (the average value in Figure 2b).

Figure 2a and Figure S8 show that there is a linear *I-V* relationship when $V_a > V_{crit}$. This linear relationship originates from the rate-limiting T1 tunneling (3D-2D tunneling; from Cr (3D) to Cr_2O_3 (2D)) for the current devices (Supporting Information G and H). Evaluating the 3D-2D tunneling,[40] we obtained analytical current density−voltage (*J-V*) characteristics, eq (H14) in the Supporting Information H. Figure 3c shows calculated *J-V* plots at different temperatures obtained from eq (H14). At 0.1 K (blue line), the current density increases linearly with V_a after 1.8 V, which corresponds to the V_F in Figure 3b where the Fermi level of Cr (source), E_F, aligns with the QW1 energy level E_{QW1} of the Cr_2O_3 layer. This value is in good agreement with the experimentally measured value of V_F = 2.03 ± 0.04 (V) (Figures 2a, 2c, and S8). For higher temperatures, 150 and 298 K, Fermi−Dirac thermal smearing is apparent around V_F (1.8 V), but the linear relationships are maintained when V_a becomes larger, Figure 3c (green and red lines).

The experimental *I-V* characteristics in Figures 2a and S8 show that the electron transport is blocked when $V_a < V_{crit}$. This voltage regime $V_a < V_{crit}$ corresponds to the energy regime $E_{QW1} < E_{QW2}$ (Figure 3b) for the QW1 to QW2 transport (T2), meaning that the T2 transport is blocked when $V_a < V_{crit}$ (equivalently, when $E_{QW1} < E_{QW2}$). Likewise, T2 is enabled when $V_a > V_{crit}$ ($E_{QW1} > E_{QW2}$). This T2 behavior can be empirically expressed by a Heaviside function centered at V_{crit} but with a finite transition width of 0.25 mV. Incorporation of this empirical Heaviside-like function to the eq (H14) produces the *J-V* characteristics in Figure 3d (red line), where the transport of thermally excited electrons (yellow line in Figure 3d) is blocked when $V_a < V_{crit}$, resulting in the cold transport at room temperature. (Here we note that this cold transport should also occur at other temperatures since regardless of the degree of the thermal smearing at different temperatures, electron transport will be blocked anyway when $V_a < V_{crit}$; see also Supporting Information K) We want to emphasize that the calculated *J-V* (red line in Figure 3d) was obtained without any parameter fitting: 1) the T1 transport was analytically obtained (eq (H14)), 2) the blocking of T2 when $V_a < V_{crit}$ and enabling it when $V_a > V_{crit}$ were deduced directly from the experimental *I-V*s (Figures 2a and S8), and 3) the calculated V_{crit} was obtained without any parameter fitting (Figure 3b and Supporting Information F). The calculated *J-V* quantitatively reproduces the full experimental *J-V* characteristics at 298 K, Figure 3e.

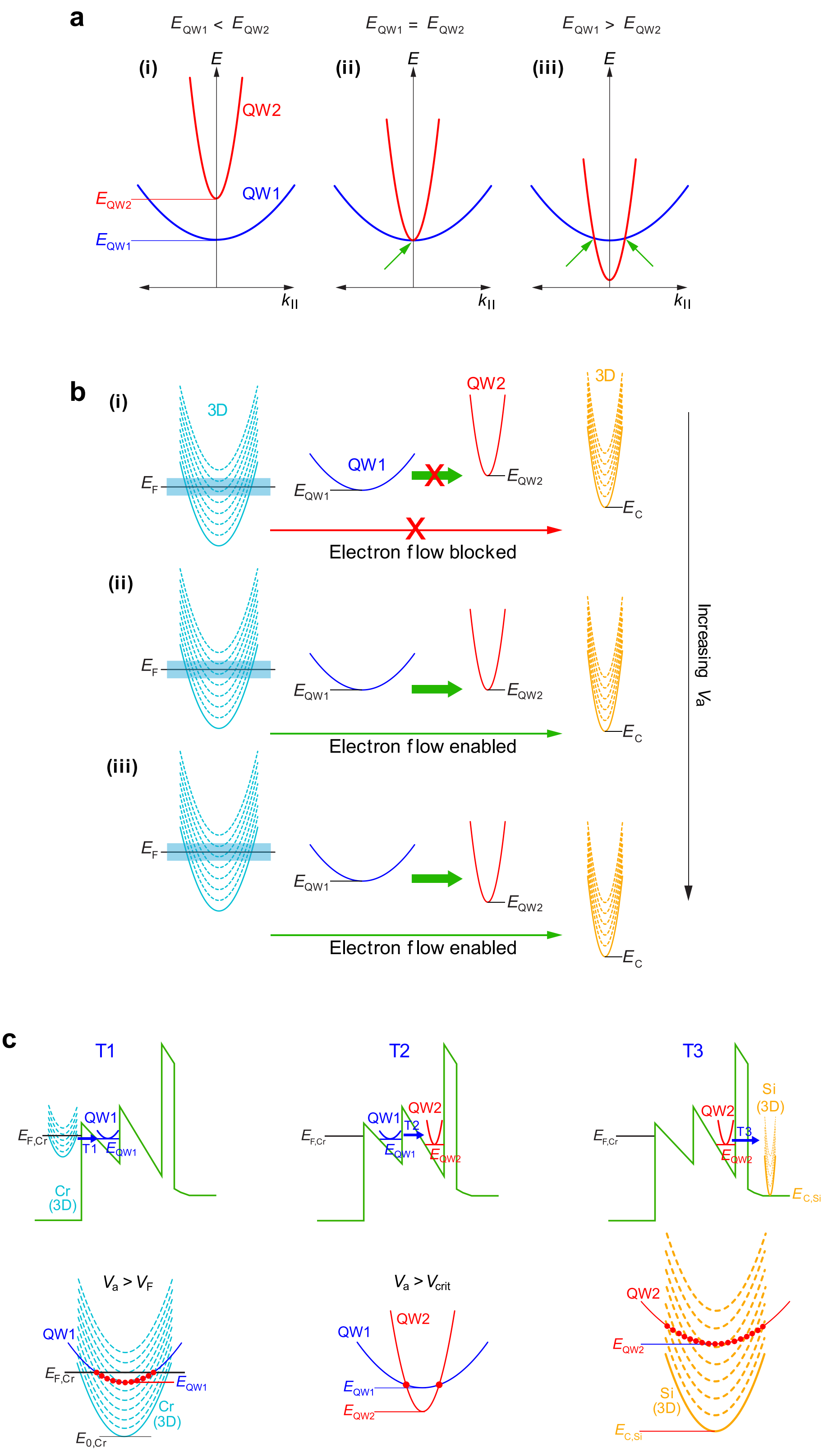

Figure 4. Schematic for the role of heterogeneity of effective electron masses and *E*-*k* relationships on electron tunneling. (a) *E*-*k* diagrams for different positions of E_{QW1} and E_{QW2}. $k_{||}$ is the transverse wave vector perpendicular to *z* direction. (i) $E_{QW1} < E_{QW2}$. No state satisfies both energy and transverse momentum conservation rules. (ii) $E_{QW1} = E_{QW2}$. The states at the bottom of QW1 and QW2 sublevels satisfy both conservation rules (indicated by green arrow). (iii) $E_{QW1} > E_{QW2}$. The states indicated by the green arrows satisfy both conservation rules. (b) *E*-*k* diagrams of QW switching. The heterogeneous double QW switch is positioned between the source (metal, 3D) and drain (semiconductor, 3D). E_F: Fermi energy of the source. E_C: Conduction band edge of the drain. The dotted *E*-*k*'s for the 3D source and the 3D drain represent the *z* component electron kinetic energies, $E_z = \frac{\hbar^2}{2m^*}k_z^2$. ($m^*$: effective electron mass; $\hbar$: reduced Planck constant; k_z: wave vector in the *z* direction (perpendicular to the QW planes)). (i)-(iii) *E*-*k* diagrams for $E_{QW1} < E_{QW2}$, $E_{QW1} = E_{QW2}$, and $E_{QW1} > E_{QW2}$, respectively. V_a: Applied voltage to the drain with source

Figure 4. continued

grounded. The QW switch blocks electron transport for (i) but enables electrons transport for (ii) and (iii). The shadow around the source Fermi energy E_F schematically represents Fermi–Dirac thermal smearing. (c) Schematic for the energy and transverse momentum conservations for the T1, T2, and T3 tunneling of the current devices (see also Figures S10 and S11). For each of T1, T2, and T3, tunneling involves electronic states that are located at the same momentum (k) space. Red dots represent the states that satisfy both energy and transverse momentum conservations. Left (T1): the tunneling occurs from the Γ band of Cr to the Γ band of Cr_2O_3 (QW1). Center (T2): the tunneling occurs from the Γ band of Cr_2O_3 (QW1) to the Γ band of SnO_x (QW2). Right (T3): the tunneling occurs from the Γ band of SnO_x (QW2) to the projected center region of the X valley of Si (100) that contains $\vec{k}_{\parallel} = (k_x, k_y) = (0, 0)$.

We note that the absence of translational symmetry in the near-amorphous Cr_2O_3 and SnO_x layers, as well as the inhomogeneities in the layers should result in a finite transition width in the current onset at V_{crit}. Quantitative understanding of the observed transition width, 0.25 mV (Figures 2a, 2d-2e, S8–S9), would require comprehensive microscopic modeling, which is beyond the scope of the current study. Nevertheless, independent of the microscopic mechanism at play at the current onset, the experimental data allows us to obtain the *necessary* condition that is required to produce the switching, *i.e.*, the blocking of electron tunneling when $V_a < V_{crit}$ and enabling electron tunneling when $V_a > V_{crit}$, which we discuss below.

We find the heterogeneity of the two QW materials plays the central role in the observed switching. Specifically, the effective electron mass of QW1 material needs to be larger than QW2 ($m^*_{QW1} > m^*_{QW2}$); for the current devices, $m^*_{Cr2O3} = 1.84m_e$[30] and $m^*_{SnOx} = 0.35m_e$,[41−44] where m_e is the electron rest mass. This can be understood from the heterogeneity of *E-k* relationships (due to $m^*_{QW1} > m^*_{QW2}$), assuming that both energy and transverse momentum conservations hold for the tunneling between QW1 and QW2, Figure 4.[40,45−49] At low voltages $V_a < V_{crit}$, where $E_{QW1} < E_{QW2}$ (Figure 4a(i)), no transport mechanism satisfying both energy and transverse momentum conservation is available until $V_a \sim V_{crit}$, whereas if V_a is at V_{crit} or larger ($V_a \geq V_{crit}$; $E_{QW1} \geq E_{QW2}$) tunneling can occur that satisfies both conservation rules (green arrows in Figures 4a(ii)-(iii)). Figure 4b shows energy diagrams when the QW switch in Figure 4a is inserted between the source and drain. The electron transport is blocked when $V_a < V_{crit}$ ($E_{QW1} < E_{QW2}$), Figure 4b(i), and it is enabled when $V_a \geq V_{crit}$ ($E_{QW1} \geq E_{QW2}$), Figures 4b(ii)-(iii). We note that if the necessary condition $m^*_{QW1} > m^*_{QW2}$ is not met, then QW switching will not occur. If the same materials are used for QW1 and QW2 (*i.e.*, $m^*_{QW1} = m^*_{QW2}$; Note: In this case, a tunneling barrier needs to be inserted between the QW1 and QW2 as otherwise, *separate* QW states (E_{QW1} and E_{QW2}) will not form), then resonance behavior will occur with negative differential conductance (NDC)[48,50] (reaches a peak in current when two subbands align, but results in NDC when they deviate from the alignment). If $m^*_{QW1} < m^*_{QW2}$, the blocking of electron transport at low voltage biases (where $E_{QW1} < E_{QW2}$) will not occur since tunneling paths always exist that satisfy both energy and transverse momentum conservation.

We note that for the transverse momentum conservation to hold the electronic states involved in the tunneling should be located in the same momentum space. For the devices in the current study, each of the T1, T2, and T3 tunneling satisfies that requirement (details in Supporting Information G and I). The momentum spaces for the materials used in this study (Cr, Cr_2O_3, SnO_x, and Si(100)) are shown in the *E-k* diagrams in Figure S11. For the current devices, the T1 tunneling (left in Figure 4c and Figure S10a) occurs from the Γ band of Cr to the Γ band of Cr_2O_3 (see the red arrows in Figures S11a and S11b). For the T2 (center in Figures 4c and Figure S10b), the tunneling occurs from the Γ band of Cr_2O_3 to the Γ band of SnO_x (see the red arrows in Figures S11b-S11d). For the T3 (right in Figure 4c and Figure S10c), the tunneling occurs from the Γ band of SnO_x to the projected center region of the X valley of Si (100) that contains $\vec{k}_{\parallel} = (k_x, k_y) = (0, 0)$ (see the red arrows in Figures S11c-S11e).

In classical electrostatic switching, such as in field-effect transistors, electron transport is controlled by increasing or decreasing the energy barrier between the source and the drain. This switching, however, is subject to intrinsic thermal broadening due to the hot electrons in the Fermi–Dirac distribution tail.[6,8−11,13,14,16−23,25,26,51−56] If a gating structure is implemented with the cold-electron QW switches, then transistors can likely be fabricated that are not subject to thermal broadening (*i.e.*, enabling an abrupt current onset). With the 0.8 K effective electron temperature demonstrated, the subthreshold slope (*SS*) of a transistor could in principle reach as low as 0.16 mV/decade at room temperature ($SS = (k_BT/q)\ \ln 10 = 0.16$ mV/decade; $k_B = 8.62 \times 10^{-5}$ [eV/K], $T = 0.8$ K, q: electron charge).[10,17,25,52,55,57−59] Further effort to build transistors utilizing the cold-electron QW switching (along with making V_{crit} low (*e.g.*, < 0.1 V) by adjusting the alignment of E_{QW1} and E_{QW2}) would thus be an attractive direction toward realizing energy-efficient integrated circuits.

In summary, we investigated QW switching in which two heterogeneous QWs are used to block or enable electron tunneling, effectively suppressing the Fermi–Dirac thermal smearing in electron transport. The room-temperature *I-V* characteristics of the fabricated devices show abrupt current jumps (switching) at the critical applied voltage $V_a = V_{crit}$, where the amount of current jump exceeds 1 mA. The abrupt current jump leads to an extremely narrow peak width in the differential conductance (*dI*/*dV*) plot, with a peak fwhm of only 0.25 mV, which corresponds to an effective electron temperature of 0.8 K at room temperature. The experimental findings are well explained by a model in which the heterogeneity of the two QW materials having different *E-k* characteristics ($m^*_{QW1} > m^*_{QW2}$) blocks electron tunneling when $E_{QW1} < E_{QW2}$ and enables electron tunneling when $E_{QW1} \geq E_{QW2}$. The observed sub-1K cold-electron switching at room temperature, along with the compatibility of this scheme with CMOS fabrication, has far-reaching potential for energy-efficient transistors and related applications.

■ ASSOCIATED CONTENT

Supporting Information

The Supporting Information is available free of charge at https://pubs.acs.org/doi/10.1021/acs.nanolett.4c03348.

Materials requirements, device layout, TEM analysis and sample preparation, *I-V* and *dI*/*dV* characteristics of the fabricated devices, calculations of QW quasi-bound states, qualitative analyses of T1, T2, and T3, analytical solution of T1 (3D-2D) tunneling, transverse momentum conservation and electronic structures, effects of layer thickness variations on V_{crit}, cold-electron switching at different temperatures, and methods of device fabrication (PDF)

AUTHOR INFORMATION

Corresponding Author

Seong Jin Koh − *Department of Materials Science and Engineering, The University of Texas at Arlington, Arlington, Texas 76019, United States*; orcid.org/0000-0001-7721-5593; Email: skoh@uta.edu

Authors

Anthony Martinez − *Department of Materials Science and Engineering, The University of Texas at Arlington, Arlington, Texas 76019, United States*; orcid.org/0000-0002-0624-4888

Pushkar K. Gothe − *Department of Materials Science and Engineering, The University of Texas at Arlington, Arlington, Texas 76019, United States*; orcid.org/0000-0002-8471-3889

Yi-De Liou − *Department of Materials Science and Engineering, The University of Texas at Arlington, Arlington, Texas 76019, United States*

Ojas T. Bhayde − *Department of Materials Science and Engineering, The University of Texas at Arlington, Arlington, Texas 76019, United States*

J. Tyler Gish − *Department of Materials Science and Engineering, Northwestern University, Evanston, Illinois 60208, United States*; orcid.org/0000-0001-8429-5800

Vinod K. Sangwan − *Department of Materials Science and Engineering, Northwestern University, Evanston, Illinois 60208, United States*; orcid.org/0000-0002-5623-5285

Michael P. Rabel − *Department of Materials Science and Engineering, The University of Texas at Arlington, Arlington, Texas 76019, United States*

Thévenin Rumende − *Department of Materials Science and Engineering, The University of Texas at Arlington, Arlington, Texas 76019, United States*

Gumaro G. Gonzalez − *Department of Materials Science and Engineering, The University of Texas at Arlington, Arlington, Texas 76019, United States*

Jiechao Jiang − *Department of Materials Science and Engineering, The University of Texas at Arlington, Arlington, Texas 76019, United States*

Ye Cao − *Department of Materials Science and Engineering, The University of Texas at Arlington, Arlington, Texas 76019, United States*; orcid.org/0000-0002-7365-7447

Pierre Darancet − *Argonne National Laboratory, Lemont, Illinois 60439, United States*; orcid.org/0000-0002-5846-1673

Efstathios Meletis − *Department of Materials Science and Engineering, The University of Texas at Arlington, Arlington, Texas 76019, United States*

Mark C. Hersam − *Department of Materials Science and Engineering, Department of Chemistry, and Department of Electrical and Computer Engineering, Northwestern University, Evanston, Illinois 60208, United States*; orcid.org/0000-0003-4120-1426

Complete contact information is available at: https://pubs.acs.org/10.1021/acs.nanolett.4c03348

Author Contributions

S.J.K. conceived the study. A.M., P.K.G., Y.-D.L., O.T.B., J.T.G., V.K.S., M.P.R., T.R., and G.G.G. fabricated devices and performed measurements and analysis. J.J. and E.M. performed the TEM analysis. S.J.K., P.D., Y.-D.L., Y.C., M.C.H., and V.K.S. developed the model. Y.-D.L., Y.C., and S.J.K. performed the numerical calculations. S.J.K. wrote the initial manuscript. M.C.H., P.D., V.K.S., and E.M. edited and contributed to the final manuscript. All authors read the manuscript and provided feedback. A.M., P.K.G., and Y.-D.L. contributed equally to this work.

Notes

The authors declare no competing financial interest.

ACKNOWLEDGMENTS

This work was primarily supported by the National Science Foundation Partnership for Research and Education in Materials (NSF DMR-2425164 and NSF DMR-2122128) and the National Science Foundation Materials Research Science and Engineering Center at Northwestern University (NSF DMR-2308691). Work performed at the Center for Nanoscale Materials, a U.S. Department of Energy Office of Science User Facility, was supported by the U.S. DOE, Office of Basic Energy Sciences, under Contract No. DE-AC02-06CH11357.

REFERENCES

(1) Likharev, K. K. Single-Electron Devices and Their Applications. *Proc. IEEE* **1999**, *87* (4), 606−632.

(2) Ray, V.; Subramanian, R.; Bhadrachalam, P.; Ma, L. C.; Kim, C. U.; Koh, S. J. CMOS-Compatible Fabrication of Room-Temperature Single-Electron Devices. *Nat. Nanotechnol.* **2008**, *3* (10), 603−608.

(3) Shibata, K.; Yoshida, M.; Hirakawa, K.; Otsuka, T.; Bisri, S. Z.; Iwasa, Y. Single PbS Colloidal Quantum Dot Transistors. *Nat. Commun.* **2023**, *14* (1), 7486.

(4) Zhang, J.; Qian, L.; Barin, G. B.; Daaoub, A. H. S.; Chen, P. P.; Müllen, K.; Sangtarash, S.; Ruffieux, P.; Fasel, R.; Sadeghi, H.; Zhang, J.; Calame, M.; Perrin, M. L. Contacting Individual Graphene Nanoribbons Using Carbon Nanotube Electrodes. *Nat. Electron.* **2023**, *6* (8), 572−581.

(5) Niu, W. H.; Sopp, S.; Lodi, A.; Gee, A.; Kong, F. M.; Pei, T.; Gehring, P.; Nägele, J.; Lau, C. S.; Ma, J.; Liu, J. Z.; Narita, A.; Mol, J.; Burghard, M.; Müllen, K.; Mai, Y. Y.; Feng, X. L.; Bogani, L. Exceptionally Clean Single-Electron Transistors from Solutions of Molecular Graphene Nanoribbons. *Nat. Mater.* **2023**, *22* (2), 180−185.

(6) Seabaugh, A. C.; Zhang, Q. Low-Voltage Tunnel Transistors for Beyond CMOS Logic. *Proc. IEEE* **2010**, *98* (12), 2095−2110.

(7) Avci, U. E.; Morris, D. H.; Young, I. A. Tunnel Field-Effect Transistors: Prospects and Challenges. *IEEE Journal of the Electron Devices Society* **2015**, *3* (3), 88−95.

(8) Cao, W.; Bu, H. M.; Vinet, M.; Cao, M.; Takagi, S.; Hwang, S.; Ghani, T.; Banerjee, K. The Future Transistors. *Nature* **2023**, *620* (7974), 501−515.

(9) Cristoloveanu, S.; Wan, J.; Zaslavsky, A. A Review of Sharp-Switching Devices for Ultra-Low Power Applications. *IEEE J. Electron Devices Soc.* **2016**, *4* (5), 215−226.

(10) Wang, S. S.; Wang, J.; Zhi, T.; Xue, J. J.; Chen, D. J.; Wang, L. H.; Zhang, R. Cold Source Field-Effect Transistors: Breaking the 60-mV/decade Switching Limit at Room Temperature. *Phys. Rep.-Rev. Sec. Phys. Lett.* **2023**, *1013*, 1−33.

(11) Yu, S. E.; Lee, H. J.; Kim, M.-g.; Im, S.; Lee, Y. T. J-MISFET Hybrid Dual-Gate Switching Device for Multifunctional Optoelec-

tronic Logic Gate Applications. *ACS Nano* **2024**, *18* (17), 11404−11415.
(12) Jones, N. The Information Factories. *Nature* **2018**, *561* (7722), 163−166.
(13) Song, S.; Rahaman, M.; Jariwala, D. Can 2D Semiconductors Be Game-Changers for Nanoelectronics and Photonics? *ACS Nano* **2024**, *18* (17), 10955−10978.
(14) Nazir, G.; Rehman, A.; Park, S. J. Energy-Efficient Tunneling Field-Effect Transistors for Low-Power Device Applications: Challenges and Opportunities. *ACS Appl. Mater. Interfaces* **2020**, *12* (42), 47127−47163.
(15) Nadeem, M.; Di Bernardo, I.; Wang, X. L.; Fuhrer, M. S.; Culcer, D. Overcoming Boltzmann's Tyranny in a Transistor via the Topological Quantum Field Effect. *Nano Lett.* **2021**, *21* (7), 3155−3161.
(16) Logoteta, D.; Cao, J.; Pala, M.; Dollfus, P.; Lee, Y.; Iannaccone, G. Cold-Source Paradigm for Steep-Slope Transistors Based on van der Waals Heterojunctions. *Phys. Rev. Res.* **2020**, *2* (4), No. 043286.
(17) Qin, L. X.; Tian, H.; Li, C. L.; Xie, Z.; Wei, Y. Q.; Li, Y.; He, J.; Yue, Y. T.; Ren, T. L. Steep Slope Field Effect Transistors Based on 2D Materials. *Adv. Electron. Mater.* **2024**, *10*, 2300625.
(18) Zhang, L. G.; Yao, G. W.; Liu, X. Y.; Liu, F. Three-Dimensional Cold Metals in Realizing Steep-Slope Transistors Based on Monolayer MoS_2. *IEEE Electron Device Lett.* **2023**, *44* (10), 1764−1767.
(19) Zhou, H.; Dong, X. P.; Prentki, R. J.; Cao, R. G.; Wang, J.; Guo, H.; Liu, F. Quantum Transport Simulations of Sub-60-mV/Decade Switching of Silicon Cold Source Transistors. *IEEE Trans. Electron Devices* **2024**, *71* (4), 2781−2788.
(20) Huang, J. K.; Wan, Y.; Shi, J. J.; Zhang, J.; Wang, Z. H.; Wang, W. X.; Yang, N.; Liu, Y.; Lin, C. H.; Guan, X. W.; Hu, L.; Yang, Z. L.; Huang, B. C.; Chiu, Y. P.; Yang, J.; Tung, V.; Wang, D. Y.; Kalantar-Zadeh, K.; Wu, T.; Zu, X. T.; Qiao, L.; Li, L. J.; Li, S. High-κ Perovskite Membranes as Insulators for Two-Dimensional Transistors. *Nature* **2022**, *605* (7909), 262−267.
(21) Li, H.; Li, Q. H.; Li, Y.; Yang, Z. M.; Quhe, R. G.; Sun, X. T.; Wang, Y. Y.; Xu, L.; Peng, L. M.; Tian, H.; Qiu, C. G.; Lu, J. Recent Experimental Breakthroughs on 2D Transistors: Approaching the Theoretical Limit. *Adv. Funct. Mater.* **2024**, *34*, 2402474.
(22) Fiori, G.; Bonaccorso, F.; Iannaccone, G.; Palacios, T.; Neumaier, D.; Seabaugh, A.; Banerjee, S. K.; Colombo, L. Electronics Based on Two-Dimensional Materials. *Nat. Nanotechnol.* **2014**, *9* (10), 768−779.
(23) Miao, J. S.; Leblanc, C.; Wang, J. J.; Gu, Y.; Liu, X. W.; Song, B. K.; Zhang, H. R.; Krylyuk, S.; Hu, W. D.; Davydov, A. V.; Back, T.; Glavin, N.; Jariwala, D. Heterojunction Tunnel Triodes Based on Two-Dimensional Metal Selenide and Three-Dimensional Silicon. *Nat. Electron.* **2022**, *5* (11), 744−751.
(24) Choi, H.; Li, J.; Kang, T.; Kang, C.; Son, H.; Jeon, J.; Hwang, E.; Lee, S. A Steep Switching WSe_2 Impact Ionization Field-Effect Transistor. *Nat. Commun.* **2022**, *13* (1), 6076.
(25) Myeong, G.; Shin, W.; Sung, K.; Kim, S.; Lim, H.; Kim, B.; Jin, T.; Park, J.; Lee, T.; Fuhrer, M. S.; Watanabe, K.; Taniguchi, T.; Liu, F.; Cho, S. Dirac-Source Diode with Sub-Unity Ideality Factor. *Nat. Commun.* **2022**, *13* (1), 4328.
(26) Shin, W.; Myeong, G.; Sung, K.; Kim, S.; Lim, H.; Kim, B.; Jin, T.; Park, J.; Watanabe, K.; Taniguchi, T.; Liu, F.; Cho, S. Steep-Slope Schottky Diode with Cold Metal Source. *Appl. Phys. Lett.* **2022**, *120* (24), No. 243506.
(27) Kim, S.; Myeong, G.; Park, J.; Jin, T.; Watanabe, K.; Taniguchi, T.; Lee, C.; Cho, S. Complementary Trilayer-Bulk Black Phosphorus Heterojunction Tunnel Field-Effect Transistor with Subthermionic Subthreshold Swing. *ACS Appl. Electron. Mater.* **2020**, *2* (11), 3491−3496.
(28) van der Wiel, W. G.; De Franceschi, S.; Elzerman, J. M.; Fujisawa, T.; Tarucha, S.; Kouwenhoven, L. P. Electron Transport Through Double Quantum Dots. *Rev. Mod. Phys.* **2003**, *75* (1), 1−22.
(29) Kouwenhoven, L. Coupled Quantum Dots as Artificial Molecules. *Science* **1995**, *268* (5216), 1440−1441.
(30) Bhadrachalam, P.; Subramanian, R.; Ray, V.; Ma, L. C.; Wang, W. C.; Kim, J.; Cho, K.; Koh, S. J. Energy-Filtered Cold Electron Transport at Room Temperature. *Nat. Commun.* **2014**, *5*, 4745.
(31) Korotkov, A. N.; Likharev, K. K. Possible Cooling by Resonant Fowler-Nordheim Emission. *Appl. Phys. Lett.* **1999**, *75* (16), 2491−2493.
(32) Korotkov, A. N.; Likharev, K. K. Cooling by Resonant Fowler-Nordheim Emission. *Physica B* **2000**, *284*, 2030−2031.
(33) Dodin, A.; Aull, B.; Kunz, R. R.; Willard, A. P. Theoretical Bounds on Electron Energy Filtering in Disordered Nanomaterials. *Nano Lett.* **2019**, *19* (12), 8441−8446.
(34) Beckers, A.; Thewissen, M.; Sorée, B. Energy Filtering in Silicon Nanowires and Nanosheets Using a Geometric Superlattice and Its Use for Steep-Slope Transistors. *J. Appl. Phys.* **2018**, *124* (14), No. 144304.
(35) van der Vaart, N. C.; Godijn, S. F.; Nazarov, Y. V.; Harmans, C. J. P. M.; Mooij, J. E.; Molenkamp, L. W.; Foxon, C. T. Resonant Tunneling Through Two Discrete Energy States. *Phys. Rev. Lett.* **1995**, *74* (23), 4702−4705.
(36) Martiradonna, L. Cold Transport at Room Temperature. *Nat. Mater.* **2014**, *13* (11), 998.
(37) Tu, K. N. Recent Advances on Electromigration in Very-Large-Scale-Integration of Interconnects. *J. Appl. Phys.* **2003**, *94* (9), 5451−5473.
(38) Conrad, H. Effects of Electric Current on Solid State Phase Transformations in Metals. *Mater. Sci. Eng. A-Struct. Mater. Prop. Microstruct. Process.* **2000**, *287* (2), 227−237.
(39) Miller, C. W.; Belyea, D. D. The Impact of Barrier Height Distributions in Tunnel Junctions. *J. Appl. Phys.* **2009**, *105* (9), No. 094505.
(40) Ohno, H.; Mendez, E. E.; Wang, W. I. Effects of Carrier Mass Differences on the Current-Voltage Characteristics of Resonant Tunneling Structures. *Appl. Phys. Lett.* **1990**, *56* (18), 1793−1795.
(41) Nagasawa, M.; Shionoya, S.; Makishima, S. Electron Effective Mass of SnO_2. *J. Phys. Soc. Jpn.* **1965**, *20* (6), 1093.
(42) Button, K. J.; Fonstad, C. G.; Dreybrodt, W. Determination of the Electron Masses in Stannic Oxide by Submillimeter Cyclotron Resonance. *Phys. Rev. B* **1971**, *4* (12), 4539−4542.
(43) Chen, R. S.; Wang, W. C.; Lu, M. L.; Chen, Y. F.; Lin, H. C.; Chen, K. H.; Chen, L. C. Anomalous Quantum Efficiency for Photoconduction and Its Power Dependence in Metal Oxide Semiconductor Nanowires. *Nanoscale* **2013**, *5* (15), 6867−6873.
(44) Borges, P. D.; Scolfaro, L. M. R.; Leite Alves, H. W.; da Silva, E. F. DFT Study of the Electronic, Vibrational, and Optical Properties of SnO_2. *Theor. Chem. Acc.* **2010**, *126* (1−2), 39−44.
(45) Lebens, J. A.; Silsbee, R. H.; Wright, S. L. Tunneling and Transverse Wave Vector Conservation in GaAs/AlGaAs Heterostructures. *Appl. Phys. Lett.* **1987**, *51* (11), 840−842.
(46) Luryi, S. Frequency Limit of Double-Barrier Resonant-Tunneling Oscillators. *Appl. Phys. Lett.* **1985**, *47* (5), 490−492.
(47) Vexler, M. I.; Illarionov, Y. Y.; Suturin, S. M.; Fedorov, V. V.; Sokolov, N. S. Tunneling of Electrons with Conservation of the Transverse Wave Vector in the Au/CaF_2/Si(111) System. *Phys. Solid State* **2010**, *52* (11), 2357−2363.
(48) Kinoshita, K.; Moriya, R.; Okazaki, S.; Zhang, Y.; Masubuchi, S.; Watanabe, K.; Taniguchi, T.; Sasagawa, T.; Machida, T. Resonant Tunneling between Quantized Subbands in van der Waals Double Quantum Well Structure Based on Few-Layer WSe_2. *Nano Lett.* **2022**, *22* (12), 4640−4645.
(49) Finley, J. J.; Teissier, R. J.; Skolnick, M. S.; Cockburn, J. W.; Roberts, G. A.; Grey, R.; Hill, G.; Pate, M. A.; Planel, R. Role of the X Minimum in Transport Through AlAs Single-Barrier Structures. *Phys. Rev. B* **1998**, *58* (16), 10619−10628.
(50) Britnell, L.; Gorbachev, R. V.; Geim, A. K.; Ponomarenko, L. A.; Mishchenko, A.; Greenaway, M. T.; Fromhold, T. M.; Novoselov, K. S.; Eaves, L. Resonant Tunnelling and Negative Differential Conductance in Graphene Transistors. *Nat. Commun.* **2013**, *4*, 1794.

https://doi.org/10.1021/acs.nanolett.4c03348
Nano Lett. 2024, 24, 13981−13990

(51) Bernstein, K.; Cavin, R. K.; Porod, W.; Seabaugh, A.; Welser, J. Device and Architecture Outlook for Beyond CMOS Switches. *Proc. IEEE* **2010**, *98* (12), 2169−2184.
(52) Liu, M. M.; Jaiswal, H. N.; Shahi, S.; Wei, S. C.; Fu, Y.; Chang, C. R.; Chakravarty, A.; Liu, X. C.; Yang, C.; Liu, Y. P.; Lee, Y. H.; Perebeinos, V.; Yao, F.; Li, H. M. Two-Dimensional Cold Electron Transport for Steep-Slope Transistors. *ACS Nano* **2021**, *15* (3), 5762−5772.
(53) Si, M. W.; Su, C. J.; Jiang, C. S.; Conrad, N. J.; Zhou, H.; Maize, K. D.; Qiu, G.; Wu, C. T.; Shakouri, A.; Alam, M. A.; Ye, P. D. Steep-Slope Hysteresis-Free Negative Capacitance MoS_2 Transistors. *Nat. Nanotechnol.* **2018**, *13* (1), 24−28.
(54) Chen, C. Y.; Zhou, W. H.; Yang, J. L.; Qu, H. Z.; Wu, Z. H.; Zeng, H. B.; Zhang, S. L. Suppressing Thermal Tail by Dirac States and High Density of States in Two-Dimensional Ag_2S toward Low-Power Electronics. *ACS Mater. Lett.* **2024**, *6* (5), 2065−2071.
(55) Qiu, C.; Liu, F.; Xu, L.; Deng, B.; Xiao, M.; Si, J.; Lin, L.; Zhang, Z.; Wang, J.; Guo, H.; Peng, H.; Peng, L.-M. Dirac-Source Field-Effect Transistors as Energy-Efficient, High-Performance Electronic Switches. *Science* **2018**, *361* (6400), 387−392.
(56) Liu, K. Y.; Lu, F.; Li, Y. Bias-Independent Subthreshold Swing in Ballistic Cold-Source Field-Effect Transistors by Drain Density-of-States Engineering. *Appl. Phys. Lett.* **2024**, *124* (5), No. 053504.
(57) Chhowalla, M.; Jena, D.; Zhang, H. Two-Dimensional Semiconductors for Transistors. *Nat. Rev. Mater.* **2016**, *1* (11), 16052.
(58) Sarkar, D.; Xie, X. J.; Liu, W.; Cao, W.; Kang, J. H.; Gong, Y. J.; Kraemer, S.; Ajayan, P. M.; Banerjee, K. A Subthermionic Tunnel Field-Effect Transistor with an Atomically Thin Channel. *Nature* **2015**, *526* (7571), 91−95.
(59) Kamaei, S.; Liu, X.; Saeidi, A.; Wei, Y. F.; Gastaldi, C.; Brugger, J.; Ionescu, A. M. Ferroelectric Gating of Two-Dimensional Semiconductors for the Integration of Steep-Slope Logic and Neuromorphic Devices. *Nat. Electron.* **2023**, *6*, 658−668.

https://doi.org/10.1021/acs.nanolett.4c03348
Nano Lett. 2024, 24, 13981−13990